HHS Public Access

Author manuscript

Magn Reson Med. Author manuscript; available in PMC 2018 July 01.

Published in final edited form as:

Magn Reson Med. 2017 July ; 78(1): 79–87. doi:10.1002/mrm.26342.

Sparse-SEMAC: Rapid and Improved SEMAC Metal Implant Imaging Using SPARSE-SENSE Acceleration

Ricardo Otazo[1,*], **Mathias Nittka**[2], **Mary Bruno**[1], **Esther Raithel**[2], **Christian Geppert**[2], **Soterios Gyftopoulos**[1], **Michael Recht**[1], and **Leon Rybak**[1]

[1]Department of Radiology, NYU School of Medicine, New York, NY, 10016, USA.

[2]Siemens Healthcare GmbH, Erlangen, Germany.

Abstract

Purpose—To develop an accelerated SEMAC metal implant MRI technique (Sparse-SEMAC) with reduced scan time and improved metal distortion correction.

Methods—Sparse-SEMAC jointly exploits the inherent sparsity along the additional phase-encoding dimension and multicoil encoding capabilities to significantly accelerate data acquisition. A prototype pulse sequence with pseudorandom k_y-k_z undersampling and an inline image reconstruction was developed for integration in clinical studies. Three patients with hip implants were imaged using the proposed Sparse-SEMAC with eight-fold acceleration and compared with the standard-SEMAC technique used in clinical studies (three-fold GRAPPA acceleration). Measurements were performed with SEMAC-encoding steps (SES)=15 for Sparse-SEMAC and SES=9 for Standard-SEMAC using high spatial resolution Proton Density (PD) and lower-resolution STIR acquisitions. Two expert musculoskeletal (MSK) radiologists performed a consensus reading to score image-quality parameters.

Results—Sparse-SEMAC enables up to eight-fold acceleration of data acquisition that results in two-fold scan time reductions, compared with Standard-SEMAC, with improved metal artifact correction for patients with hip implants without degrading spatial resolution.

Conclusion—The high acceleration enabled by Sparse-SEMAC would enable clinically feasible examination times with improved correction of metal distortion.

Keywords

metallic implants; metal artifacts; SPARSE-SENSE; iterative reconstruction; parallel imaging

INTRODUCTION

MRI offers several advantages for assessing both normal anatomy and pathology in proximity to metallic implants, including lack of ionizing radiation and superior soft-tissue resolution and contrast (1). The ability to correctly diagnose certain soft tissue complications inherent in orthopedic joint replacement procedures can help direct treatment, and in some

[*]Correspondence to: Ricardo Otazo, PhD, Center for Biomedical Imaging, Department of Radiology, New York University School of Medicine, 660 First Ave, 4th Floor, New York, NY 10016, USA. Tel: 212-263-4842; Fax: 212-263-7541; ricardo.otazo@nyumc.org.

cases, obviate the need for revision surgery. However, there are substantial challenges for MRI around metal. The presence of metallic implants introduces susceptibility-induced magnetic field inhomogeneities, and consequently frequency offsets, which interfere with the MR imaging procedure and result in a variety of image artifacts (2,3). Typical artifacts include regions with no signal as a result of intravoxel dephasing (T_2^* and shift of image pixels along both the readout direction (in-plane distortion) and slice direction (through-plane distortion), leading to dark regions caused by signal loss in one case and bright regions caused by signal pile-up in the other case.

Several approaches have been explored to improve MRI near metallic implants. Turbo spin echo (TSE) pulse sequences refocus the dephased spins and can recover most of the signal loss caused by intravoxel dephasing. View-angle tilting (VAT) (4) compensates for in-plane distortions by using an additional readout gradient applied along the slice-selective dimension to gather all of the excited spins within the radiofrequency (RF) bandwidth, and therefore remove pixel shifts along the readout dimension. Through-plane distortion can be corrected by using additional encoding. With multiple-acquisition with variable resonances image combination (MAVRIC), multiple nonselective three-dimensional (3D) TSE acquisitions at different center frequencies are performed (5). Because of the absence of a slice-selection gradient, each acquisition in MAVRIC will only collect signal within the excited RF bandwidth, such that the measurements at different frequencies can be combined into a final image that covers a wider range of off-resonant signals. In slice encoding for metal artifact correction (SEMAC), slice-selective excitation and 3D encoding for each slice are used to resolve distortions along the through-plane dimension (6). MAVRIC and SEMAC can also be combined to relieve the restrictions of the nonselective excitation of MAVRIC (7). Both MAVRIC and SEMAC have been proven to achieve significant reduction of metal-related distortions in clinical studies (8–11). However, the additional phase-encoding steps result in significant increases in imaging time, which has limited broad clinical application.

Parallel imaging and partial Fourier are usually employed to accelerate SEMAC data acquisition (12), but the acquisition time is still lengthy for routine clinical studies and ultimately limited by signal-to-noise ratio (SNR). As a consequence, the number of SEMAC-encoding steps is commonly sacrificed to have a clinically acceptable time, which reduces the ability to resolve metal-related distortions. Hexagonal k-space undersampling (13) was recently proposed to increase the acceleration capability for SEMAC imaging by reducing the signal overlap in *y-z* space for each slice (*y:* standard phase encoding, *z:* additional phase encoding) in a similar fashion to the UNFOLD (14) method for dynamic imaging.

SEMAC is a natural candidate for the application of compressed sensing (15) as a result of the inherent sparsity of the additional phase-encoding dimension and the opportunity to perform two-dimensional (2D) acceleration along the two phase-encoding dimensions. Compressed sensing was first applied to SEMAC using a 3D wavelet transform to enforce sparsity in the solution, resulting in two-fold acceleration factors in spine examinations (16). Higher accelerations can be achieved by jointly exploiting image sparsity and parallel imaging encoding. Previous work performed a sequential two-step combination, in which

coil-by-coil sparse reconstruction was used in a first step, resulting in regularly aliased images that were then unaliased using standard SENSE reconstruction in a second step (17). The two-step approach resulted in four-fold accelerated knee scans with respect to a conventional MAVRIC-SL acquisition with a partial Fourier factor of 1.8 and $4/\pi$ elliptical encoding (the total acceleration with respect to a fully sampled acquisition was approximately 8).

In this work, we present a highly accelerated SEMAC metal imaging technique called Sparse-SEMAC to enable rapid clinical examinations with high spatial resolution and enhanced distortion correction. Sparse-SEMAC uses a SPARSE-SENSE reconstruction approach (18,19) to enforce joint multicoil sparsity, which was demonstrated to perform better than separate coil-by-coil sparse reconstruction. We demonstrate the feasibility of eight-fold accelerated Sparse-SEMAC in experiments with prospective undersampling in the hip and compare the performance against standard SEMAC accelerated with parallel imaging.

METHODS

SPARSE-SENSE Acceleration for SEMAC

The proposed Sparse-SEMAC method is based on the following components to jointly exploit image sparsity and parallel imaging encoding for SEMAC:

- Inherent sparsity along the SEMAC encoding dimension (z): The extra phase-encoding dimension to resolve metal artifacts (z) is inherently sparse, as only a few pixels around the metal implant will cause large spatial distortions, while most of the pixels will result in very limited or no spatial distortion (Fig. 1).
- Poisson-disk undersampling pattern (20) in the k_y-k_z plane (Fig. 2): The random distribution of k-space samples produce the required incoherent aliasing artifacts for sparsity-based reconstruction, but with limited distance between adjacent k-samples to constrain the conditioning of the parallel imaging acquisition model. This approach has proven to be a good compromise between incoherence and conditioning of the inverse problem, leading to improved performance for combinations of compressed sensing and parallel imaging (21).
- *Joint multicoil sparse reconstruction*: Based on the SPARSE-SENSE approach (18,19), image reconstruction is performed by solving the following optimization problem: $min_m \| Em - d \|_2^2 + \lambda \| m \|_1$, where m is the 3D image to be reconstructed for each slice (the third dimension corresponds to the extra phase encoding to resolve metal artifacts), E is the multicoil encoding model that includes the undersampled Fourier transform and coil sensitivities (SENSE model), and d is the undersampled k-space data.

The left-hand side term (l_2-norm) enforces multicoil data consistency by minimizing the distance between the undersampled multicoil k-space representation of the solution m and the acquired multicoil data y, and the right-hand side term (l_1-norm) enforces sparsity on the solution m by knocking out the low-value coefficients and keeping the high-value

coefficients. The algorithm promotes joint multicoil sparsity rather than coil-by-coil sparsity, as m represents the contribution from all coils given by the SENSE model. The parameter λ weights the contribution of the l_1-norm term against the l_2-norm term.

Accelerated Pulse Sequence

A prototype Sparse-SEMAC pulse sequence was developed based on a conventional multislice TSE sequence with a short tau inversion recovery (STIR) module for fat suppression and additional gradients for VAT and SEMAC encoding (5). The two-dimensional phase-encoding matrix along k_y and k_z implements the Poisson disk distribution described previously (Fig. 2). A central 24×8 k_y-k_z region is fully sampled for autocalibration of coil sensitivities, which reduces the effective acceleration. This is approximately compensated by an elliptical scanning scheme that omits sampling of the outer edges of k-space. The TSE acquisition scheme requires segmentation of the phase-encoding matrix, with each segment being assigned to a certain echo position within the echo train. The color pattern in Figure 2 shows how the conventional segmentation along k_y is extended to the k_z dimension for SEMAC encoding, ensuring that the central k-space segment is filled with echoes sampled at the given echo time (TE). The resulting matrix consists of N blocks aligned along k_y, N=2×echo train length (ETL), fulfilling the boundary condition that each block contains the same number of points, such that an integer number of echo trains will finally cover all points in k-space.

Inline Image Reconstruction

SPARSE-SENSE image reconstruction was performed using a fast iterative soft-thresholding algorithm (FISTA) (22), which is simpler and thus faster than gradient-descent type of algorithms, because the gradient of the l_1-norm term does not need to be computed explicitly and can be replaced by a soft-thresholding operation. Coil sensitivity maps were computed using low-resolution images obtained from the fully sampled central k-space region by dividing each low-resolution image by the sum of squares of all low-resolution images. A redundant 3D Haar wavelet transform was used to further sparsify the SEMAC data set. To increase reconstruction speed, the multidimensional reconstruction problem (*x-y-z-s*, where s represents each slice) was decoupled in independent subproblems that can be reconstructed in parallel. Specifically, the accelerated *y-z* plane was reconstructed in parallel for each *x* and *s* points after applying an inverse fast Fourier transform (FFT) operation along the fully sampled dimension k_x. The parameter λ was set to 1% of the maximum signal intensity in the zero-filled FFT reconstruction of the undersampled data. Following SPARSE-SENSE reconstruction, image combination along the z dimension was performed using sum of squares as described in the standard SEMAC method (6). A prototype image reconstruction algorithm was implemented in C++ using multithreaded programming and integrated on a standard clinical scanner reconstruction computer.

Ex Vivo Knee Experiment with Retrospective Undersampling

An ex vivo experiment on a human knee cadaver with a total joint replacement (CoCr alloy) was performed to compare different retrospective undersampling factors against conventional FFT reconstruction of the fully sampled data. We selected an ex vivo study, because the acquisition of an in vivo fully sampled reference with high spatial resolution and

sufficient number of *z*-points is very challenging because of the long scan time, which inevitably results in motion-related artifacts. Fully sampled SEMAC data were acquired on a 1.5 Tesla (T) scanner (MAGNETOM Aera, Siemens Healthcare, Erlangen, Germany) using a four-element coil array. Scan time was 19 min and the relevant imaging parameters included 16 metal-encoding points, field of view (FOV) 180 × 180 mm^2, 320 × 256 in-plane image matrix, 27 slices with 4-mm thickness, in which each slice is excited at a bandwidth of 1 kHz without overlap (off-resonance coverage of ± 13 kHz). The fully sampled data were retrospectively undersampled by factors of 4, 8, and 12 using the Poisson disk approach and reconstructed using the Sparse-SEMAC algorithm. For comparison purposes, the data set with retrospective eight-fold undersampling was reconstructed using coil-by-coil sparse reconstruction. The reconstructions with retrospective undersampling were performed in MATLAB (MathWorks, Natick, Massachusetts, USA).

Accelerated In Vivo Hip Experiments

Three patients with total hip arthroplasties were imaged on a 1.5T scanner (MAGNETOM Aera, Siemens Healthcare, Erlangen, Germany) using view-angle tilting (VAT), Standard-SEMAC (three-fold GRAPPA acceleration only), and Sparse-SEMAC (eight-fold SPARSE-SENSE acceleration). Images were acquired with PD and STIR contrast in coronal orientation with the following imaging parameters: FOV = 260 × 260 mm^2, image matrix=384 × 384 (PD) and 256 × 256 (STIR), ETL=19 (PD) and 11 (STIR), 27 slices, slice thickness=3.5 mm, TE/repetition time (TR)=30/4000 ms, and inversion time (TI)=145 ms. Standard-SEMAC employed nine SES and the scan time was 7 min 58 s for PD contrast and 9 min 46 s for STIR contrast. Sparse-SEMAC employed 15 SES and the scan time was 4 min 7 s for PD and 5 min 6 s for STIR. The reconstruction parameter λ that weights the contribution of the sparsity term relative to parallel imaging data consistency (see equation in “Joint Multicoil Sparse Reconstruction” section) was defined to be proportional to the noise level of the undersampled images. For the same acceleration factor, the difference would be given by the baseline SNR. Because the baseline SNR of PD images is approximately twice the SNR of STIR images, λ for PD was chosen to be half of the one used for STIR. λ=0.002 M_0 was used for STIR, where M_0 is the maximum value of the standard Fourier transform reconstruction of the undersampled data. This value was selected qualitatively among five different possibilities (0.01, 0.005, 0.002, 0.001, and 0.005) by assessing the removal of aliasing artifacts and blurring. Accordingly, λ=0.001 M_0 was used for PD. To assess the effects of sparse sampling and reconstruction of Sparse-SEMAC on spatial resolution, we simulated a low-resolution Standard-SEMAC acquisition that would match the scan time of the accelerated Sparse-SEMAC acquisition. This was accomplished by discarding high-frequency k-space points along the phase-encoding dimension of the high-resolution PD Standard-SEMAC acquisition. The low-resolution SEMAC acquisition was then compared against the Sparse-SEMAC reconstruction.

Image Quality Analysis

Standard-SEMAC and Sparse-SEMAC results were anonymized and presented in a random order to two board-certified musculoskeletal (MSK) radiologists for evaluation of image quality. The two readers performed a consensus scoring of the following parameters using a 5-point Likert scale, in which 1 implies the best result and 5 the worst result of conspicuity

of metal/bone interface, blurring, visualization of surrounding soft tissues, homogeneity of fat suppression, and overall image quality.

RESULTS

Ex Vivo Knee Experiment with Retrospective Undersampling

The performance of Sparse-SEMAC decreased with increasing undersampling factors, as expected, but resulted in adequate image quality up to an undersampling factor of 8 (Fig. 3). Residual aliasing artifacts along the phase-encoding dimension (horizontal dimension in Fig. 3) and slight blurring around the metal implants were noticed in the reconstruction for 12-fold undersampling. Based on these findings, we selected R=8 as the undersampling factor to be used in the accelerated pulse sequence. As expected, joint multicoil sparse reconstruction (SPARSE-SENSE) outperformed coil-by-coil sparse reconstruction (Fig. 4), which was consistent with previous findings in different applications such as brain (18) and cardiac (19) imaging. In particular, coil-by-coil sparse reconstruction resulted in residual aliasing artifacts and slight blurring in the neighborhood of the metal implant as well as more artificial shading. These types of artifacts are common when a sparse reconstruction breaks down.

Accelerated In Vivo Hip Experiments

Sparse-SEMAC resulted in markedly improved performance over Standard-SEMAC in terms of metal artifact correction, despite the two-fold decrease in scan time (Figs. 5–8, Table 1). For high-resolution PD imaging, Sparse-SEMAC does not introduce notable blurring in the muscle in comparison to Standard-SEMAC, and the interface between implant and tissue is actually better defined in terms of metal artifacts (see zoomed images at the acetabular cup in Fig. 5). The improvement in the implant definition is the result of the higher number of SEMAC-encoding steps used in Sparse-SEMAC (15) compared with Standard-SEMAC (9), and not a consequence of the sparsity-based reconstruction. Sparse-SEMAC presents much higher spatial resolution than a scan time–matched lower-resolution Standard-SEMAC (Fig. 6), which shows that the sparsity-based approach in fact reconstructs images with similar spatial resolution to the one of a lengthy conventional imaging approach. For STIR images, which were acquired with lower resolution as a result of SNR limitations, Sparse-SEMAC significantly improved the correction of metal distortions without degrading spatial resolution (Figs. 7 and 8). STIR contrast is of particular clinical interest, as it enables accurate detection of edema and identification of intra- or extra-articular fluid collections—many in the setting of arthroplasty. The improved correction of metal distortion resulted in visualization of small structures in the region of the metallic implant that are not visible in the Standard-SEMAC images and are consistent with X-ray images (Fig. 8). The consensus scoring yielded improved image-quality parameters for Sparse-SEMAC, particularly in the conspicuity of metal/bone interface and overall image quality (Table 1).

DISCUSSION

MR imaging in the presence of metallic hardware has taken on greater importance, given the aging population and the greater proportion of patients with painful total joint arthroplasties requiring diagnosis and treatment. Although great inroads have been made with respect to designing specific imaging sequences to meet these challenges, the clinical utility of these sequences is in doubt because of long imaging times. We decided to apply SPARSE-SENSE acceleration to the SEMAC approach to reduce imaging time without sacrificing image quality.

Previous work to accelerate SEMAC proposed using compressed sensing alone (16) or compressed sensing followed by parallel imaging (17). The latter represents a sequential combination of compressed sensing and parallel imaging, which might not exploit all of the synergies between these two complementary approaches. With this sequential technique, the reduction in incoherent aliasing artifacts provided by parallel imaging is not employed in the compressed sensing step, and the noise regularization capabilities of compressed sensing reconstruction are not used in the parallel imaging step. Our proposed joint reconstruction based on the SPARSE-SENSE approach (19) is designed to fully exploit these synergies in a single reconstruction approach that enforces joint multicoil sparsity. Using this method, we were able to achieve up to eight-fold accelerations, which represents a two-fold improvement over the sequential approach given in (17).

An important point in the application of compressed sensing techniques is the selection of the reconstruction parameter (or regularization parameter) that weights the contribution of the sparsity constraint relative to the data acquisition model. This parameter depends on the sparsity level (the minimum number of transform coefficients to adequately represent the image) and the noise level in the undersampled images. A higher value may cause blurring and synthetic features in the reconstructed images, which at first glance might deliver the wrong impression that the method is not working. In this work, we have weighted the reconstruction parameter inversely proportional to the baseline SNR, to account for the differences in SNR between PD and STIR acquisitions. Using the STIR parameter for reconstruction of PD data would likely result in blurring artifacts, and vice versa, using the PD parameter for STIR data would result in residual aliasing artifacts. Even though we are not proposing an automated method to select the parameter, the experiments performed in this work give an idea of how to reconstruct each contrast.

We applied the proposed Sparse-SEMAC to clinical cases and compared the results to Standard-SEMAC as it is employed in our institution, both with respect to imaging times as well as image quality. Our current clinical protocol for SEMAC in the hip uses nine SEMAC-encoding steps. Even though a higher number would be beneficial for artifact reduction, this parameter was limited to keep the examination time within tolerable limits. Therefore, it was possible in the hip to spend part of the time gained by Sparse-SEMAC to increase to 15 phase-encoding steps, thereby improving artifact reduction in addition to shortening the scan time (Figs. 5–8). Increasing the number of steps beyond 15 does not improve metal reduction in any substantial way, as demonstrated before in (23). In general,

depending on the application, the user has the freedom to choose between increased imaging speed and/or increased SEMAC encoding for improved metal artifact correction.

The results for the image assessment portion of our study demonstrated comparable overall image quality for the Sparse-SEMAC images as compared with the conventional SEMAC images, with improvements in certain respects. The clinical readers found the overall image quality to be better for Sparse-SEMAC images of the hip, with improved conspicuity of the metal-bone interface and homogeneity of fat saturation. This was felt to be the case in the hip in part because of the opportunity to increase to 15 phase-encoding steps discussed previously.

This work presented results using non-fat-suppressed PD and STIR contrasts. STIR has demonstrated superior fat suppression with less dependency on magnetic field homogeneity (24,25). Because the detection of edema, both within the marrow and surrounding soft-tissue envelope, in addition to the identification of intra- or extra -articular fluid collections, is vital to the diagnosis of many pathologies in the setting of arthroplasty, a decision was made several years ago at our institution to employ SEMAC solely for the purposes of obtaining STIR images in the most valuable orientation plane for a particular joint (coronal in the hip). Furthermore, because of the intrinsic low SNR of STIR imaging, acquisition times are considerably longer than non-fat-suppressed pulse sequences, and consequently makes it highly attractive for acceleration. However, from an image reconstruction perspective, STIR images present a greater challenge, as their relatively low SNR as a result of both the fat suppression and inversion recovery mechanism make them less compressible. The high acceleration in Sparse-SEMAC can enable us to image with various contrasts in additional planes. Further work in this respect is underway at our institution.

CONCLUSIONS

This work presents Sparse-SEMAC, a highly accelerated SEMAC technique that jointly exploits sparsity along the extra phase-encoding dimension and parallel imaging, for fast and robust MRI near orthopedic metallic implants. A prototype Sparse-SEMAC pulse sequence and an inline reconstruction were implemented and compared with Standard-SEMAC in clinical knee and hip examinations. Sparse-SEMAC with eight-fold acceleration is able to reduce the scan time by an effective factor of approximately 2, and/or improve metal artifact correction by adding more metal encoding steps with respect to Standard-SEMAC. The improved trade-off between scan time and metal artifact correction enabled by Sparse-SEMAC would facilitate the use of SEMAC-like techniques in clinical routine imaging.

ACKNOWLEDGMENTS

The work was performed under the rubric of the Center for Advanced Imaging Innovation and Research (CAI^{2}R), a NIBIB Biomedical Technology Resource Center (NIH P41 EB017183).

REFERENCES

1. Eustace S, Goldberg R, Williamson D, Melhem ER, Oladipo O, Yucel EK, Jara H. MR imaging of soft tissues adjacent to orthopaedic hardware: techniques to minimize susceptibility artefact. Clin Radiol. 1997; 52:589–594. [PubMed: 9285418]

2. Ludeke KM, Roschmann P, Tischler R. Susceptibility artefacts in NMR imaging. Magn Reson Imaging. 1985; 3:329–343. [PubMed: 4088009]

3. Hargreaves BA, Worters PW, Pauly KB, Pauly JM, Koch KM, Gold GE. Metal-induced artifacts in MRI. Am J Roentgenol. 2011; 197(3):547–555. [PubMed: 21862795]

4. Cho ZH, Kim DJ, Kim YK. Total inhomogeneity correction including chemical shifts and susceptibility by view angle tilting. Med Phys. 1988; 15(1):7–11. [PubMed: 3352554]

5. Koch KM, Lorbiecki JE, Hinks RS, King KF. A multispectral three-dimensional acquisition technique for imaging near metal implants. Magn Reson Med. 2009; 61(2):381–390. [PubMed: 19165901]

6. Lu W, Pauly KB, Gold GE, Pauly JM, Hargreaves BA. SEMAC: slice encoding for metal artifact correction in MRI. Magn Reson Med. 2009; 62(1):66–76. [PubMed: 19267347]

7. Koch KM, Brau AC, Chen W, Gold GE, Hargreaves BA, Koff M, McKinnon GC, Potter HG, King KF. Imaging near metal with a MAVRIC-SEMAC hybrid. Magn Reson Med. 2011; 65:71–82. [PubMed: 20981709]

8. Chen CA, Chen W, Goodman SB, et al. New MR imaging methods for metallic implants in the knee: artifact correction and clinical impact. J Magn Reson Imaging. 2011; 33:1121–1127. [PubMed: 21509870]

9. Hayter CL, Koff MF, Shah P, Koch KM, Miller TT, Potter HG. MRI after arthroplasty: comparison of MAVRIC and conventional fast spin-echo techniques. Am J Roentgenol. 2011; 197:W405–W411. [PubMed: 21862766]

10. Lee YH, Lim D, Kim E, Kim S, Song H-T, Suh J-S. Usefulness of slice encoding for metal artifact correction (SEMAC) for reducing metallic artifacts in 3-T MRI. Magn Reson Imaging. 2013; 31:703–706. [PubMed: 23290476]

11. Sutter R, Ulbrich EJ, Jellus V, Nittka M, Pfirrmann CWA. Reduction of metal artifacts in patients with total hip arthroplasty with slice-encoding metal artifact correction and view-angle tilting MR imaging. Radiology. 2012; 265:204–214. [PubMed: 22923720]

12. Hargreaves BA, Chen W, Lu W, Alley MT, Gold GE, Brau AC, Pauly JM, Pauly KB. Accelerated slice encoding for metal artifact correction. J Magn Reson Imaging. 2010; 31(4):987–996. [PubMed: 20373445]

13. Sveinsson B, Worters PW, Gold GE, Hargreaves BA. Hexagonal undersampling for faster MRI near metallic implants. Magn Reson Med. 2015; 73(2):662–668. [PubMed: 24549782]

14. Madore B, Glover GH, Pelc NJ. Unaliasing by Fourier-encoding the overlaps using the temporal dimension (UNFOLD), applied to cardiac imaging and fMRI. Magn Reson Med. 1999; 42(5):813–828. [PubMed: 10542340]

15. Lustig M, Donoho D, Pauly JM. Sparse MRI: the application of compressed sensing for rapid MR imaging. Magn Reson Med. 2007; 58(6):1182–1195. [PubMed: 17969013]

16. Worters PW, Sung K, Stevens KJ, Koch KM, Hargreaves BA. Compressed-sensing multispectral imaging of the postoperative spine. J Magn Reson Imaging. 2013; 37(1):243–248. [PubMed: 22791572]

17. Koch, KM., King, KF. Combined parallel imaging and compressed sensing on 3D multi-spectral imaging near metal implants.. Proceedings of the 19th Annual Meeting of ISMRM; Montreal. 2011; p. 3172

18. Liang D, Liu B, Wang J, Ying L. Accelerating SENSE using compressed sensing. Magn Reson Med. 2009; 62(6):1574–1584. [PubMed: 19785017]

19. Otazo R, Kim D, Axel L, Sodickson DK. Combination of compressed sensing and parallel imaging for highly accelerated first-pass cardiac perfusion MRI. Magn Reson Med. 2010; 64(3):767–776. [PubMed: 20535813]

20. Cook RL. Stochastic sampling in computer graphics. ACM Trans Graphics. 1986; 5(1):51–72.

21. Lustig, M., Alley, MT., Vasanawala, S., Donoho, D., Pauly, JM. L1-SPIRiT: autocalibrating parallel imaging compressed sensing.. Proceedings of the 17th Annual Meeting of ISMRM; Honolulu, HI. 2009; p. 379

22. Beck A, Teboulle M. Fast gradient-based algorithms for constrained total variation image denoising and deblurring problems. IEEE Trans Image Process. 2009; 18(11):2419–2434. [PubMed: 19635705]

23. Ai, T., Goerner, F., Padua, A., Nittka, M., Li, X., Runge, V. The optimizations of SEMAC-VAT technique for magnetic resonance imaging of total knee prosthesis: comparison of 1.5T and 3T for different metal materials.. Proceedings of the 21st Annual Meeting of ISMRM; Salt Lake City, UT. 2013; 2013. p. 3488

24. Viano AM, Gronemeyer SA, Haliloglu M, Hoffer FA. Improved MR imaging for patients with metallic implants. Magn Reson Imaging. 2000; 18:287–295. [PubMed: 10745138]

25. Ulbrich EJ, Sutter R, Aguiar RF, Nittka M, Pfirrmann CW. STIR sequence with increased receiver bandwidth of the inversion pulse for reduction of metallic artifacts. Am J Roentgenol. 2012; 199(6):W735–W742. [PubMed: 23169747]

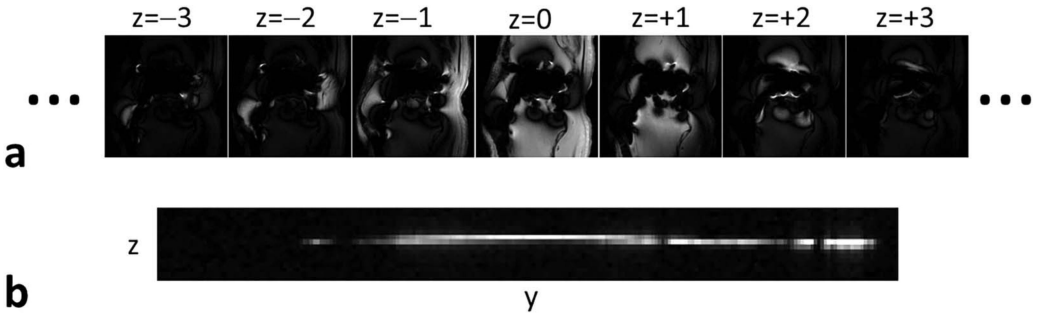

FIG. 1.

Inherent sparsity of SEMAC images along the extra phase-encoding dimension used to resolve metal artifacts (*z*). z is sparse, as only a few pixels around the metal implant suffer from large spatial distortions, whereas most of the pixels require only one or two *z*-encodings. The bottom figure shows the *y*-*z* plane for the central *x* position. The proposed Sparse-SEMAC method exploits *y*-*z* sparsity to reduce the number of samples in k_y-k_z space and thus accelerate data acquisition.

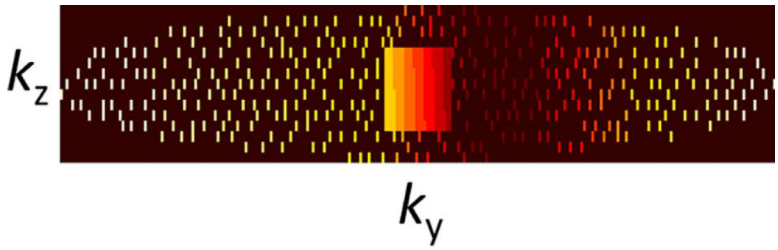

FIG. 2.

k_y-k_z phase-encoding acquisition scheme with eight-fold acceleration using a Poisson-disk undersampling pattern (black: nonsampled). The central 24×8 region is fully sampled for coil sensitivity calibration. k-space edges are skipped to compensate for the additional encoding at the center. Colors encode the position of each sample within the echo train (dark red: early echos, white: late echos). The acquisition parameters for this case are TE=38 ms, echo spacing=7.5 ms, echo train length 13, number of k_y points=256, number of k_z points=15.

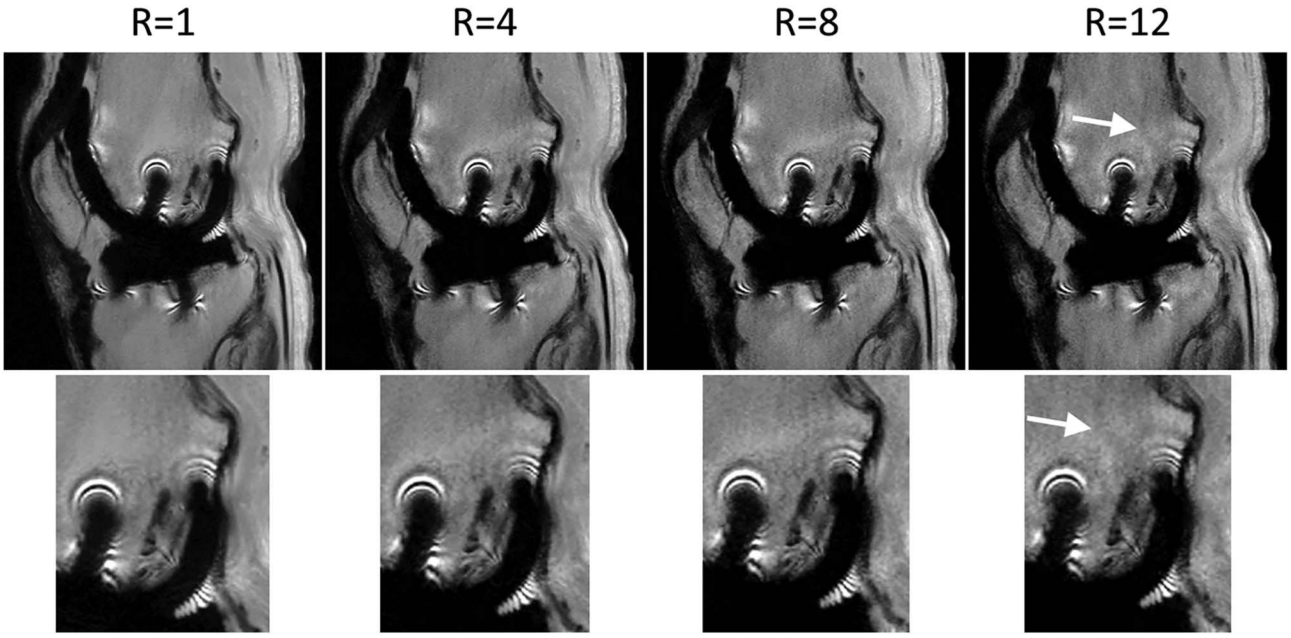

FIG. 3.

Ex vivo experiment with retrospective acceleration for a representative slice. The fully sampled data (R=1) was retrospectively undersampled by factors R=4, 8, and 12 using the Poisson-disk pattern, and reconstructed using the SPARSE-SENSE algorithm in MATLAB. Adequate image quality can be obtained up to R=8. R=12 shows residual aliasing artifacts (arrow) and slight blurring in the region around the metal implant (zoomed images in the bottom row). Note that these images were reconstructed offline without gradient warp correction.

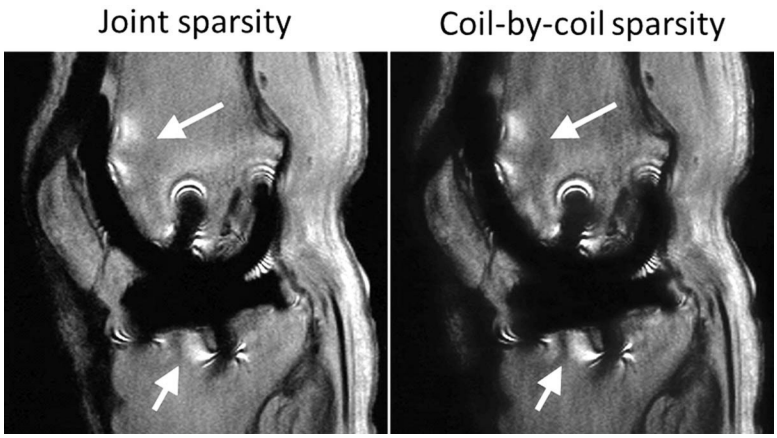

FIG. 4.

SPARSE-SENSE reconstruction using joint sparsity and coil-by-coil sparse reconstruction of the ex vivo data set with retrospective eight-fold undersampling. The coil-by-coil sparse reconstruction presents residual aliasing artifacts (arrows) and slight blurring–particularly in the region around the metal implant. Note that these images were reconstructed offline without gradient warp correction.

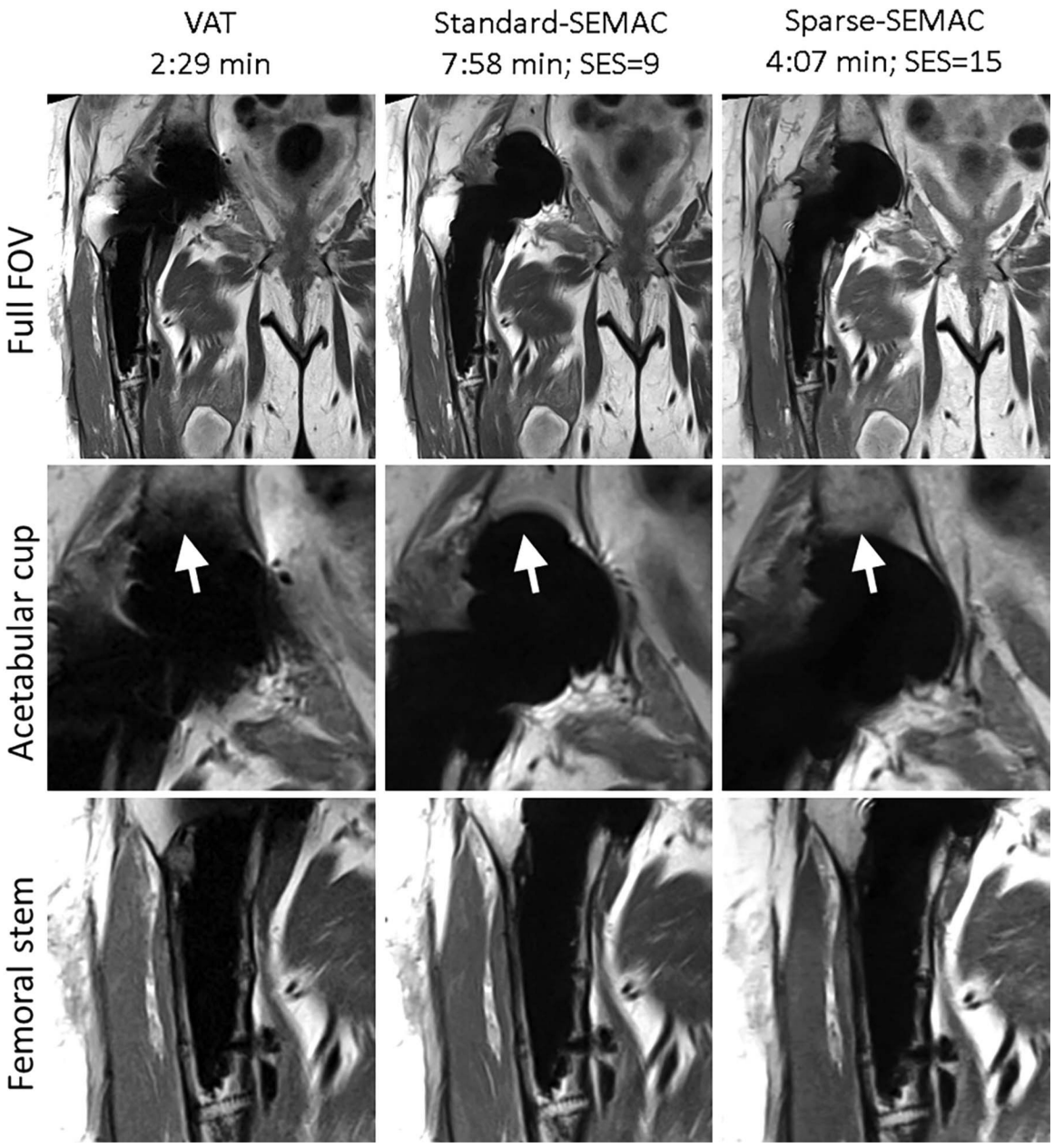

FIG. 5.

VAT, Standard-SEMAC, and Sparse-SEMAC with PD contrast at very high in-plane resolution ($0.67 \times 0.67 mm^2$) in a patient with total hip arthroplasties (Patient A in Table 1). Sparse-SEMAC presents improved correction of metal distortions (arrows) in half the scan time with respect to Standard-SEMAC. The arrows also show that Sparse-SEMAC enables imaging closer to the metal implant than Standard-SEMAC. The Sparse-SEMAC benefits come with no appreciable cost in image quality (implant-tissue interfaces at the acetabular cup and femoral stem are clearly defined, and the muscle presents similar blurring to Standard-SEMAC).

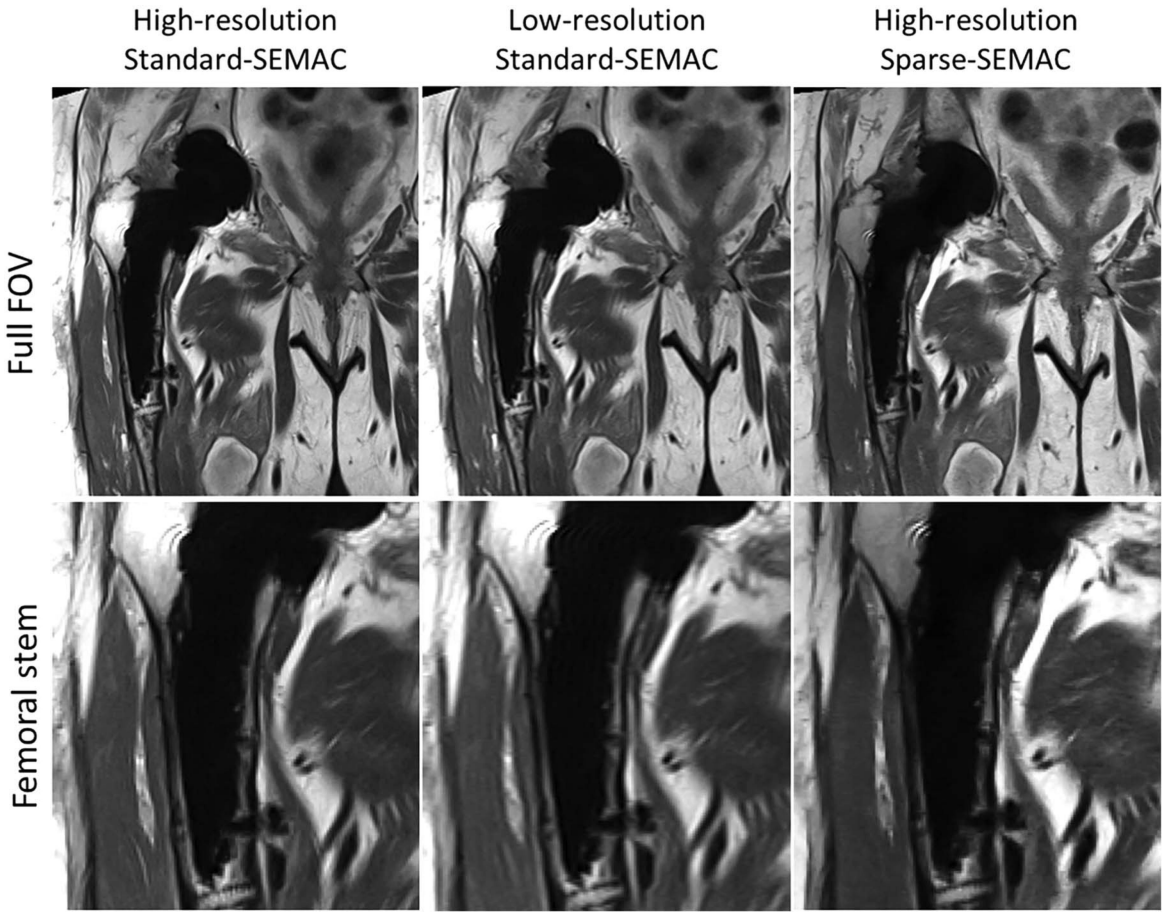

FIG. 6.

Original high-resolution Standard-SEMAC, simulated low-resolution Standard-SEMAC (the original high-resolution Standard-SEMAC was downsampled by a factor of 2 along the phase-encoding dimension to match the acquisition time of high-resolution Sparse-SEMAC), and Sparse-SEMAC on Patient A (Fig. 5). Sparse-SEMAC presents significantly higher spatial resolution than the time-matched, lower-resolution Standard-SEMAC experiment.

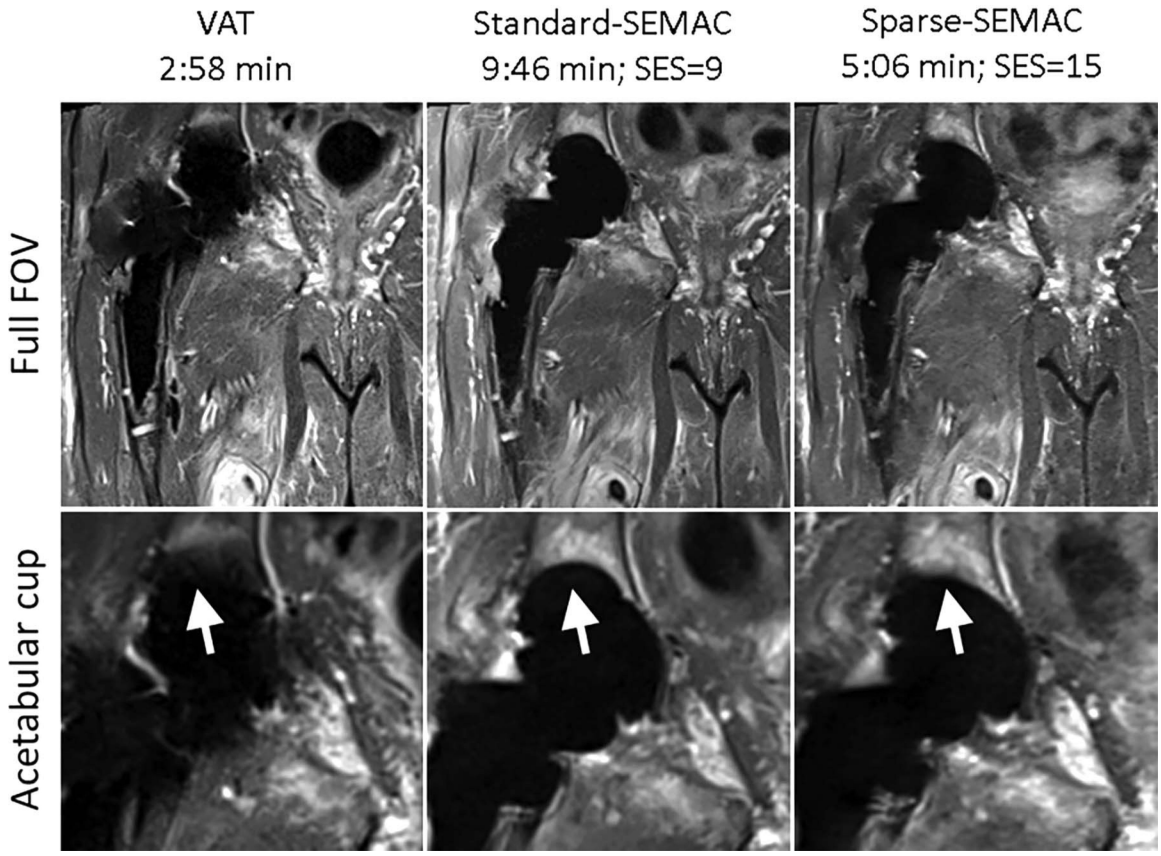

FIG. 7.

VAT, Standard-SEMAC, and Sparse-SEMAC with STIR contrast in a patient with total hip arthroplasties (Patient A in Table 1, same patient as in Figs. 5 and 6). The proposed highly accelerated Sparse-SEMAC technique significantly improves image quality close to the implant (see arrows at the acetabular cup) in approximately half the time of the Standard-SEMAC.

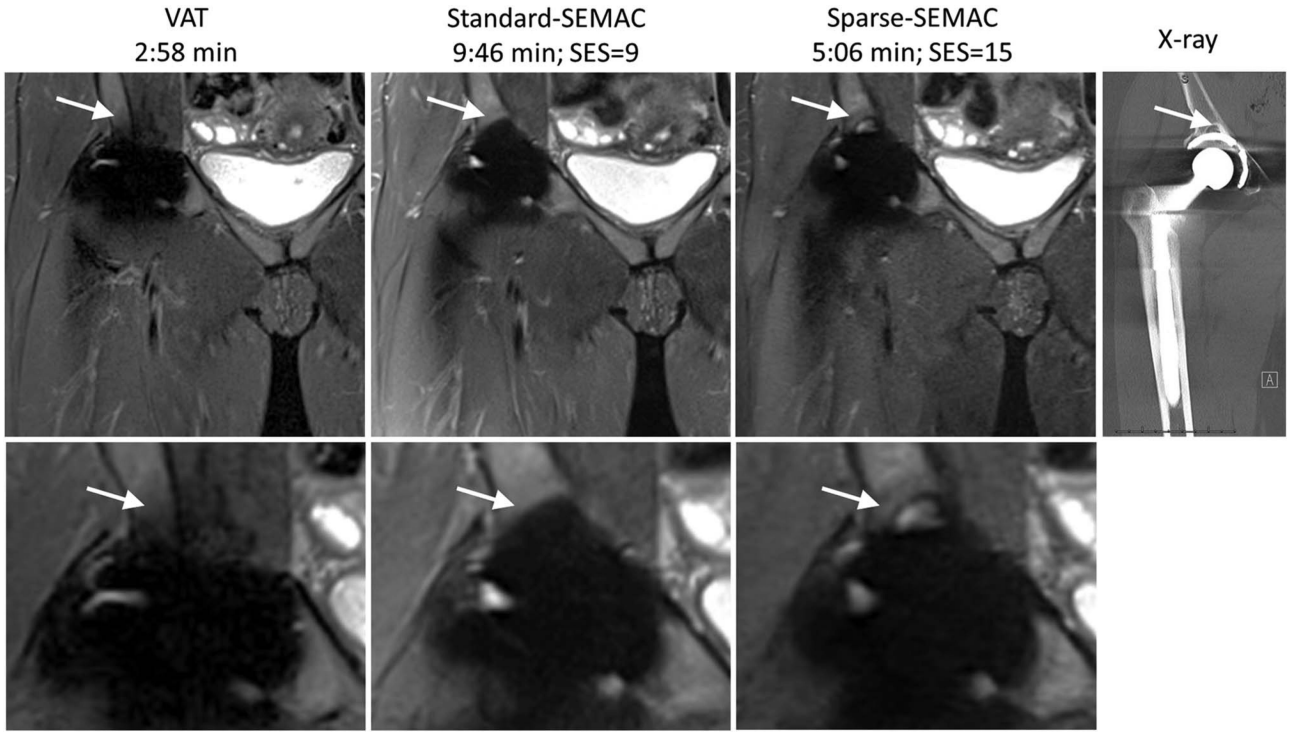

FIG. 8.

VAT, Standard-SEMAC, Sparse-SEMAC with STIR contrast, and corresponding X-ray images in a patient with total hip arthroplasties (Patient C). The improved correction of metal distortions in Sparse-SEMAC improves spatial resolution around the metallic implant matching the X-ray image (arrows).

Table 1

Image Quality Scores for In Vivo Hip Experiments with STIR Contrast Using a 5-Point Likert Scale (1 Implies Best Result and 5 Worst Result)

		Conspicuity of metal/bone interface	Blurring	Visualization of surrounding soft tissues	Homogeneity of fat suppression	Overall image quality
Patient A	Standard-SEMAC	4	2	2	2	3
	Sparse-SEMAC	2	3	2	2	2
Patient B	Standard-SEMAC	4	1	2	3	3
	Sparse-SEMAC	2	1	2	2	2
Patient C	Standard-SEMAC	4	1	2	2	4
	Sparse-SEMAC	2	1	2	2	2

Note: Sparse-SEMAC markedly improved the correction of metal artifacts compared with Standard-SEMAC, as expected, because of the larger number of SEMAC-encoding steps (SES). Sparse-SEMAC used 15 SES, whereas Standard-SEMAC used only 9 SES.